Search for thermal X-ray features from the Crab nebula with the Hitomi soft X-ray spectrometer*

Hitomi Collaboration, Felix AHARONIAN,[1] Hiroki AKAMATSU,[2]
Fumie AKIMOTO,[3] Steven W. ALLEN,[4,5,6] Lorella ANGELINI,[7] Marc AUDARD,[8]
Hisamitsu AWAKI,[9] Magnus AXELSSON,[10] Aya BAMBA,[11,12]
Marshall W. BAUTZ,[13] Roger BLANDFORD,[4,5,6] Laura W. BRENNEMAN,[14]
Gregory V. BROWN,[15] Esra BULBUL,[13] Edward M. CACKETT,[16]
Maria CHERNYAKOVA,[1] Meng P. CHIAO,[7] Paolo S. COPPI,[17,18] Elisa COSTANTINI,[2]
Jelle DE PLAA,[2] Cor P. DE VRIES,[2] Jan-Willem DEN HERDER,[2] Chris DONE,[19]
Tadayasu DOTANI,[20] Ken EBISAWA,[20] Megan E. ECKART,[7] Teruaki ENOTO,[21,22]
Yuichiro EZOE,[23] Andrew C. FABIAN,[24] Carlo FERRIGNO,[8] Adam R. FOSTER,[14]
Ryuichi FUJIMOTO,[25] Yasushi FUKAZAWA,[26] Akihiro FURUZAWA,[27]
Massimiliano GALEAZZI,[28] Luigi C. GALLO,[29] Poshak GANDHI,[30]
Margherita GIUSTINI,[2] Andrea GOLDWURM,[31,32] Liyi GU,[2] Matteo GUAINAZZI,[33]
Yoshito HABA,[34] Kouichi HAGINO,[20] Kenji HAMAGUCHI,[7,35] Ilana M. HARRUS,[7,35]
Isamu HATSUKADE,[36] Katsuhiro HAYASHI,[20] Takayuki HAYASHI,[37]
Kiyoshi HAYASHIDA,[38] Junko S. HIRAGA,[39] Ann HORNSCHEMEIER,[7]
Akio HOSHINO,[40] John P. HUGHES,[41] Yuto ICHINOHE,[23] Ryo IIZUKA,[20]
Hajime INOUE,[42] Yoshiyuki INOUE,[20] Manabu ISHIDA,[20] Kumi ISHIKAWA,[20]
Yoshitaka ISHISAKI,[23] Jelle KAASTRA,[2,43] Tim KALLMAN,[7] Tsuneyoshi KAMAE,[11]
Jun KATAOKA,[44] Satoru KATSUDA,[45] Nobuyuki KAWAI,[46] Richard L. KELLEY,[7]
Caroline A. KILBOURNE,[7] Takao KITAGUCHI,[26] Shunji KITAMOTO,[40]
Tetsu KITAYAMA,[47] Takayoshi KOHMURA,[48] Motohide KOKUBUN,[20]
Katsuji KOYAMA,[49] Shu KOYAMA,[20] Peter KRETSCHMAR,[50] Hans A. KRIMM,[51,52]
Aya KUBOTA,[53] Hideyo KUNIEDA,[37] Philippe LAURENT,[31,32] Shiu-Hang LEE,[21]
Maurice A. LEUTENEGGER,[7] Olivier LIMOUSIN,[32] Michael LOEWENSTEIN,[7]
Knox S. LONG,[54] David LUMB,[33] Greg MADEJSKI,[4] Yoshitomo MAEDA,[20]
Daniel MAIER,[31,32] Kazuo MAKISHIMA,[55] Maxim MARKEVITCH,[7]
Hironori MATSUMOTO,[38] Kyoko MATSUSHITA,[56] Dan MCCAMMON,[57]
Brian R. MCNAMARA,[58] Missagh MEHDIPOUR,[2] Eric D. MILLER,[13]
Jon M. MILLER,[59] Shin MINESHIGE,[21] Kazuhisa MITSUDA,[20]
Ikuyuki MITSUISHI,[37] Takuya MIYAZAWA,[60] Tsunefumi MIZUNO,[26]
Hideyuki MORI,[7] Koji MORI,[36,†] Koji MUKAI,[7,35] Hiroshi MURAKAMI,[61]
Richard F. MUSHOTZKY,[62] Takao NAKAGAWA,[20] Hiroshi NAKAJIMA,[38]
Takeshi NAKAMORI,[63] Shinya NAKASHIMA,[55] Kazuhiro NAKAZAWA,[11]
Kumiko K. NOBUKAWA,[64] Masayoshi NOBUKAWA,[65] Hirofumi NODA,[66,67]
Hirokazu ODAKA,[6] Takaya OHASHI,[23] Masanori OHNO,[26] Takashi OKAJIMA,[7]

Naomi OTA,[64] Masanobu OZAKI,[20] Frits PAERELS,[68] Stéphane PALTANI,[8]
Robert PETRE,[7] Ciro PINTO,[24] Frederick S. PORTER,[7] Katja POTTSCHMIDT,[7,35]
Christopher S. REYNOLDS,[62] Samar SAFI-HARB,[69] Shinya SAITO,[40]
Kazuhiro SAKAI,[7] Toru SASAKI,[56] Goro SATO,[20] Kosuke SATO,[56] Rie SATO,[20]
Toshiki SATO,[23,20] Makoto SAWADA,[70] Norbert SCHARTEL,[50]
Peter J. SERLEMTSOS,[7] Hiromi SETA,[23] Megumi SHIDATSU,[55]
Aurora SIMIONESCU,[20] Randall K. SMITH,[14] Yang SOONG,[7] Łukasz STAWARZ,[71]
Yasuharu SUGAWARA,[20] Satoshi SUGITA,[46] Andrew SZYMKOWIAK,[17]
Hiroyasu TAJIMA,[72] Hiromitsu TAKAHASHI,[26] Tadayuki TAKAHASHI,[20]
Shin'ichiro TAKEDA,[60] Yoh TAKEI,[20] Toru TAMAGAWA,[55] Takayuki TAMURA,[20]
Takaaki TANAKA,[49] Yasuo TANAKA,[73] Yasuyuki T. TANAKA,[26]
Makoto S. TASHIRO,[74] Yuzuru TAWARA,[37] Yukikatsu TERADA,[74]
Yuichi TERASHIMA,[9] Francesco TOMBESI,[7,62] Hiroshi TOMIDA,[20] Yohko TSUBOI,[45]
Masahiro TSUJIMOTO,[20,†] Hiroshi TSUNEMI,[38] Takeshi Go TSURU,[49]
Hiroyuki UCHIDA,[49] Hideki UCHIYAMA,[75] Yasunobu UCHIYAMA,[40]
Shutaro UEDA,[20] Yoshihiro UEDA,[21] Shin'ichiro UNO,[76] C. Megan URRY,[17]
Eugenio URSINO,[28] Shin WATANABE,[20] Norbert WERNER,[77,78,26]
Dan R. WILKINS,[4] Brian J. WILLIAMS,[54] Shinya YAMADA,[23] Hiroya YAMAGUCHI,[7]
Kazutaka YAMAOKA,[37] Noriko Y. YAMASAKI,[20] Makoto YAMAUCHI,[36]
Shigeo YAMAUCHI,[64] Tahir YAQOOB,[35] Yoichi YATSU,[46] Daisuke YONETOKU,[25]
Irina ZHURAVLEVA,[4,5] Abderahmen ZOGHBI,[59] Nozomu TOMINAGA,[79,80] and
Takashi J. MORIYA[81]

[1]Dublin Institute for Advanced Studies, 31 Fitzwilliam Place, Dublin 2, Ireland
[2]SRON Netherlands Institute for Space Research, Sorbonnelaan 2, 3584 CA Utrecht, The Netherlands
[3]Department of Physics, Nagoya University, Furo-cho, Chikusa-ku, Nagoya, Aichi 464-8601, Japan
[4]Kavli Institute for Particle Astrophysics and Cosmology, Stanford University, 452 Lomita Mall, Stanford, CA 94305, USA
[5]Department of Physics, Stanford University, 382 Via Pueblo Mall, Stanford, CA 94305, USA
[6]SLAC National Accelerator Laboratory, 2575 Sand Hill Road, Menlo Park, CA 94025, USA
[7]NASA, Goddard Space Flight Center, 8800 Greenbelt Road, Greenbelt, MD 20771, USA
[8]Department of Astronomy, University of Geneva, ch. d'Écogia 16, CH-1290 Versoix, Switzerland
[9]Department of Physics, Ehime University, Bunkyo-cho, Matsuyama, Ehime 790-8577, Japan
[10]Department of Physics and Oskar Klein Center, Stockholm University, 106 91 Stockholm, Sweden
[11]Department of Physics, The University of Tokyo, 7-3-1 Hongo, Bunkyo-ku, Tokyo 113-0033, Japan
[12]Research Center for the Early Universe, School of Science, The University of Tokyo, 7-3-1 Hongo, Bunkyo-ku, Tokyo 113-0033, Japan
[13]Kavli Institute for Astrophysics and Space Research, Massachusetts Institute of Technology, 77 Massachusetts Avenue, Cambridge, MA 02139, USA
[14]Harvard-Smithsonian Center for Astrophysics, 60 Garden Street, Cambridge, MA 02138, USA
[15]Lawrence Livermore National Laboratory, 7000 East Avenue, Livermore, CA 94550, USA
[16]Department of Physics and Astronomy, Wayne State University, 666 W. Hancock St, Detroit, MI 48201, USA
[17]Department of Physics, Yale University, New Haven, CT 06520-8120, USA
[18]Department of Astronomy, Yale University, New Haven, CT 06520-8101, USA
[19]Centre for Extragalactic Astronomy, Department of Physics, University of Durham, South Road, Durham, DH1 3LE, UK

[20]Japan Aerospace Exploration Agency, Institute of Space and Astronautical Science, 3-1-1 Yoshino-dai, Chuo-ku, Sagamihara, Kanagawa 252-5210, Japan

[21]Department of Astronomy, Kyoto University, Kitashirakawa-Oiwake-cho, Sakyo-ku, Kyoto, Kyoto 606-8502, Japan

[22]The Hakubi Center for Advanced Research, Kyoto University, Yoshida-honmachi, Sakyo-ku, Kyoto, Kyoto 606-8501, Japan

[23]Department of Physics, Tokyo Metropolitan University, 1-1 Minami-Osawa, Hachioji, Tokyo 192-0397, Japan

[24]Institute of Astronomy, University of Cambridge, Madingley Road, Cambridge, CB3 0HA, UK

[25]Faculty of Mathematics and Physics, Kanazawa University, Kakuma-machi, Kanazawa, Ishikawa 920-1192, Japan

[26]School of Science, Hiroshima University, 1-3-1 Kagamiyama, Higashi-Hiroshima, Hiroshima 739-8526, Japan

[27]Fujita Health University, 1-98 Dengakugakubo, Kutsukake-cho, Toyoake, Aichi 470-1192, Japan

[28]Physics Department, University of Miami, 1320 Campo Sano Dr., Coral Gables, FL 33146, USA

[29]Department of Astronomy and Physics, Saint Mary's University, 923 Robie Street, Halifax, NS, B3H 3C3, Canada

[30]Department of Physics and Astronomy, University of Southampton, Highfield, Southampton, SO17 1BJ, UK

[31]Laboratoire APC, 10 rue Alice Domon et Léonie Duquet, 75013 Paris, France

[32]CEA Saclay, 91191 Gif sur Yvette, France

[33]European Space Research and Technology Center, Keplerlaan 1 2201 AZ Noordwijk, The Netherlands

[34]Department of Physics and Astronomy, Aichi University of Education, 1 Hirosawa, Igaya-cho, Kariya, Aichi 448-8543, Japan

[35]Department of Physics, University of Maryland Baltimore County, 1000 Hilltop Circle, Baltimore, MD 21250, USA

[36]Department of Applied Physics and Electronic Engineering, University of Miyazaki, 1-1 Gakuen Kibanadai-Nishi, Miyazaki, Miyazaki 889-2192, Japan

[37]Department of Physics, Nagoya University, Furo-cho, Chikusa-ku, Nagoya, Aichi 464-8602, Japan

[38]Department of Earth and Space Science, Osaka University, 1-1 Machikaneyama-cho, Toyonaka, Osaka 560-0043, Kyoto, Japan

[39]Department of Physics, Kwansei Gakuin University, 2-1 Gakuen, Sanda, Hyogo 669-1337, Japan

[40]Department of Physics, Rikkyo University, 3-34-1 Nishi-Ikebukuro, Toshima-ku, Tokyo 171-8501, Japan

[41]Department of Physics and Astronomy, Rutgers University, 136 Frelinghuysen Road, Piscataway, NJ 08854, USA

[42]Meisei University, 2-1-1 Hodokubo, Hino, Tokyo 191-8506, Japan

[43]Leiden Observatory, Leiden University, PO Box 9513, 2300 RA Leiden, The Netherlands

[44]Research Institute for Science and Engineering, Waseda University, 3-4-1 Ohkubo, Shinjuku-ku, Tokyo 169-8555, Japan

[45]Department of Physics, Chuo University, 1-13-27 Kasuga, Bunkyo-ku, Tokyo 112-8551, Japan

[46]Department of Physics, Tokyo Institute of Technology, 2-12-1 Ookayama, Meguro-ku, Tokyo 152-8550, Japan

[47]Department of Physics, Toho University, 2-2-1 Miyama, Funabashi, Chiba 274-8510, Japan

[48]Department of Physics, Tokyo University of Science, 2641 Yamazaki, Noda, Chiba 278-8510, Japan

[49]Department of Physics, Kyoto University, Kitashirakawa-Oiwake-Cho, Sakyo-ku, Kyoto, Kyoto 606-8502, Japan

[50]European Space Astronomy Center, Camino Bajo del Castillo, s/n., 28692 Villanueva de la Cañada, Madrid, Spain

[51]Universities Space Research Association, 7178 Columbia Gateway Drive, Columbia, MD 21046, USA

[52]National Science Foundation, 4201 Wilson Blvd, Arlington, VA 22230, USA

[53] Department of Electronic Information Systems, Shibaura Institute of Technology, 307 Fukasaku, Minuma-ku, Saitama, Saitama 337-8570, Japan

[54] Space Telescope Science Institute, 3700 San Martin Drive, Baltimore, MD 21218, USA

[55] Institute of Physical and Chemical Research, 2-1 Hirosawa, Wako, Saitama 351-0198, Japan

[56] Department of Physics, Tokyo University of Science, 1-3 Kagurazaka, Shinjuku-ku, Tokyo 162-8601, Japan

[57] Department of Physics, University of Wisconsin, Madison, WI 53706, USA

[58] Department of Physics and Astronomy, University of Waterloo, 200 University Avenue West, Waterloo, Ontario, N2L 3G1, Canada

[59] Department of Astronomy, University of Michigan, 1085 South University Avenue, Ann Arbor, MI 48109, USA

[60] Okinawa Institute of Science and Technology Graduate University, 1919-1 Tancha, Onna-son, Kunigami-gun, Okinawa 904-0495, Japan

[61] Faculty of Liberal Arts, Tohoku Gakuin University, 2-1-1 Tenjinzawa, Izumi-ku, Sendai, Miyagi 981-3193, Japan

[62] Department of Astronomy, University of Maryland, College Park, MD 20742, USA

[63] Faculty of Science, Yamagata University, 1-4-12 Kojirakawa-machi, Yamagata, Yamagata 990-8560, Japan

[64] Department of Physics, Nara Women's University, Kitauoyanishi-machi, Nara, Nara 630-8506, Japan

[65] Department of Teacher Training and School Education, Nara University of Education, Takabatake-cho, Nara, Nara 630-8528, Japan

[66] Frontier Research Institute for Interdisciplinary Sciences, Tohoku University, 6-3 Aramakiazaaoba, Aoba-ku, Sendai, Miyagi 980-8578, Japan

[67] Astronomical Institute, Tohoku University, 6-3 Aramakiazaaoba, Aoba-ku, Sendai, Miyagi 980-8578, Japan

[68] Astrophysics Laboratory, Columbia University, 550 West 120th Street, New York, NY 10027, USA

[69] Department of Physics and Astronomy, University of Manitoba, Winnipeg, MB R3T 2N2, Canada

[70] Department of Physics and Mathematics, Aoyama Gakuin University, 5-10-1 Fuchinobe, Chuo-ku, Sagamihara, Kanagawa 252-5258, Japan

[71] Astronomical Observatory of Jagiellonian University, ul. Orla 171, 30-244 Kraków, Poland

[72] Institute for Space-Earth Environmental Research, Nagoya University, Furo-cho, Chikusa-ku, Aichi 464-8601, Japan

[73] Max Planck Institute for Extraterrestrial Physics, Giessenbachstrasse 1, 85748 Garching, Germany

[74] Department of Physics, Saitama University, 255 Shimo-Okubo, Sakura-ku, Saitama, 338-8570, Japan

[75] Faculty of Education, Shizuoka University, 836 Ohya, Suruga-ku, Shizuoka 422-8529, Japan

[76] Faculty of Health Sciences, Nihon Fukushi University , 26-2 Higashi Haemi-cho, Handa, Aichi 475-0012, Japan

[77] MTA-Eötvös University Lendület Hot Universe Research Group, Pázmány Péter sétány 1/A, Budapest, 1117, Hungary

[78] Department of Theoretical Physics and Astrophysics, Faculty of Science, Masaryk University, Kotlářská 2, Brno, 611 37, Czech Republic

[79] Department of Physics, Faculty of Science and Engineering, Konan University, 8-9-1 Okamoto, Kobe, Hyogo 658-8501, Japan

[80] Kavli Institute for the Physics and Mathematics of the Universe (WPI), The University of Tokyo, 5-1-5 Kashiwanoha, Kashiwa, Chiba 277-8583, Japan

[81] National Astronomical Observatory of Japan, 2-21-1 Osawa, Mitaka, Tokyo 181-8588, Japan

*The corresponding authors are Masahiro TSUJIMOTO, Koji MORI, Shiu-Hang LEE, Hiroya YAMAGUCHI, Nozomu TOMINAGA, Takashi J. MORIYA, Toshiki SATO, Cor P. DE VRIES, and Ryo IIZUKA.

†E-mail: tsujimot@astro.isas.jaxa.jp, mori@astro.miyazaki-u.ac.jp

Abstract

The Crab nebula originated from a core-collapse supernova (SN) explosion observed in 1054 AD. When viewed as a supernova remnant (SNR), it has an anomalously low observed ejecta mass and kinetic energy for an Fe-core-collapse SN. Intensive searches have been made for a massive shell that solves this discrepancy, but none has been detected. An alternative idea is that SN 1054 is an electron-capture (EC) explosion with a lower explosion energy by an order of magnitude than Fe-core-collapse SNe. X-ray imaging searches were performed for the plasma emission from the shell in the Crab outskirts to set a stringent upper limit on the X-ray emitting mass. However, the extreme brightness of the source hampers access to its vicinity. We thus employed spectroscopic technique using the X-ray micro-calorimeter on board the Hitomi satellite. By exploiting its superb energy resolution, we set an upper limit for emission or absorption features from as yet undetected thermal plasma in the 2–12 keV range. We also re-evaluated the existing Chandra and XMM-Newton data. By assembling these results, a new upper limit was obtained for the X-ray plasma mass of $\lesssim 1\,M_\odot$ for a wide range of assumed shell radius, size, and plasma temperature values both in and out of collisional equilibrium. To compare with the observation, we further performed hydrodynamic simulations of the Crab SNR for two SN models (Fe-core versus EC) under two SN environments (uniform interstellar medium versus progenitor wind). We found that the observed mass limit can be compatible with both SN models if the SN environment has a low density of $\lesssim 0.03\,\mathrm{cm}^{-3}$ (Fe core) or $\lesssim 0.1\,\mathrm{cm}^{-3}$ (EC) for the uniform density, or a progenitor wind density somewhat less than that provided by a mass loss rate of $10^{-5}\,M_\odot\,\mathrm{yr}^{-1}$ at $20\,\mathrm{km\,s}^{-1}$ for the wind environment.

Key words: instrumentation: spectrographs — ISM: individual (Crab nebula) — ISM: supernova remnants — methods: observational

1 Introduction

Out of some 400[1] Galactic supernova remnants (SNRs) detected in X-rays and γ-rays (Ferrand & Safi-Harb 2012), about 10% of them lack the shell that is one of the defining characteristics of SNRs. They are often identified instead as pulsar wind nebulae (PWNe), systems that are powered by the rotational energy loss of a rapidly rotating neutron star generated as a consequence of a core-collapse supernova (SN) explosion.

The lack of a shell in these sources deserves wide attention, since it is a key to unveiling the causes behind the variety of observed phenomena in SNRs. In this pursuit, it is especially important to interpret observations in the context of the evolution from SNe to SNRs, not just a taxonomy of SNRs. Observed results of SNRs do exhibit imprints of their progenitors, explosion mechanisms, and surrounding environment (Hughes et al. 1995; Yamaguchi et al. 2014a). Recent rapid progress in simulation studies of the stellar evolution of progenitors, SN explosions, and the

hydrodynamic development of SNRs makes it possible to gain insights about SNe from SNR observations.

The Crab nebula is one such source. It is an observational standard for X-ray and γ-ray flux and time (Kirsch et al. 2005; Jahoda et al. 2006; Terada et al. 2008; Kaastra et al. 2009; Weisskopf et al. 2010; Madsen et al. 2015). As a PWN, the Crab exhibits typical X-ray and γ-ray luminosities for its spin-down luminosity (Possenti et al. 2002; Mattana et al. 2009; Kargaltsev et al. 2012) and a typical morphology (Ng & Romani 2008; Bamba et al. 2010). It has also played many iconic roles in the history of astronomy, such as giving observational proof (Staelin & Reifenstein 1968; Lovelace et al. 1968) for the birth of a neutron star in SN explosions (Baade & Zwicky 1934) and linking modern and ancient astronomy by its association with a historical SN in 1054 documented primarily in Oriental records (Lundmark 1921; Stephenson & Green 2002; Rudie et al. 2008).

This astronomical icon, however, is known to be anomalous when viewed as an SNR. Besides having no detected shell, it has an uncomfortably small observed ejecta mass of $4.6 \pm 1.8\,M_\odot$ (Fesen et al. 1997), kinetic energy of $\lesssim 1 \times 10^{50}$ erg (Davidson & Fesen 1985), and a maximum

---

[1] See ⟨http://www.physics.umanitoba.ca/snr/SNRcat/⟩ for the high-energy catalogues of SNRs and the latest statistics.

velocity of only $2500 \, \mathrm{km \, s^{-1}}$ (Sollerman et al. 2000), all of which are far below the values expected for a typical core-collapse SN.

One idea to reconcile this discrepancy is that there is a fast and thick shell yet to be detected, which carries a significant fraction of the mass and kinetic energy (Chevalier 1977). If the free expansion velocity is $10^4 \, \mathrm{km \, s^{-1}}$, the shell radius has grown to 10 pc over 10^3 yr. Intensive attempts have been made to detect such a shell with radio (Frail et al. 1995), Hα (Tziamtzis et al. 2009), and X-ray observations (Mauche & Gorenstein 1985; Predehl & Schmitt 1995; Seward et al. 2006), but without success.

Another idea is that the SN explosion was indeed anomalous to begin with. Nomoto et al. (1982) proposed that SN 1054 was an electron-capture (EC) SN, which is caused by the endothermic reaction of electrons captured in an O–Ne–Mg core, in contrast to the photo-dissociation in an Fe core for the normal core-collapse SN. Electron-capture SNe are considered to be caused by an intermediate (8–$10 \, M_\odot$) mass progenitor in the asymptotic giant branch (AGB) phase. Simulations based on first-principle calculations (Kitaura et al. 2006; Janka et al. 2008) show that an explosion takes place with a small energy of $\sim 10^{50}$ erg, presumably in a dense circumstellar environment, as a result of mass loss caused by a slow but dense stellar wind. This idea matches well with the aforementioned observations of the Crab, plus the richness of the He abundance (MacAlpine & Satterfield 2008), an extreme brightness in the historical records (Sollerman et al. 2001; Tominaga et al. 2013; Moriya et al. 2014), and the observed nebular size (Yang & Chevalier 2015). If this is the case, we should rather search for the shell much closer to the Crab.

The X-ray band is most suited to searching for the thermal emission from the 10^6–10^8 K plasma expected from the shocked material forming a shell. In the past, telescopes with a high spatial resolution were used to set an upper limit on the thermal X-ray emission from the Crab (Mauche & Gorenstein 1985; Predehl & Schmitt 1995; Seward et al. 2006). High-contrast imaging is required to minimize the contamination by scattered X-rays by the telescope itself and the interstellar dust around the Crab. Still, the vicinity of the Crab is inaccessible with these imaging techniques because of the overwhelmingly bright and non-uniform flux of the PWN.

Here, we present the result of a spectroscopic search for the thermal plasma using the soft X-ray spectrometer (SXS) on board the Hitomi satellite (Takahashi et al. 2016). The SXS is a non-dispersive high-resolution spectrometer, offering high-contrast spectroscopy to discriminate the thermal emission or absorption lines from the bright featureless spectrum of the PWN. This technique allows access to the Crab's vicinity and is complementary to the existing imaging results.

The goals of this paper are (1) to derive a new upper limit with the spectroscopic technique for the X-ray emitting plasma, (2) to assemble the upper limits by various techniques evaluated under the same assumptions, and (3) to compare with the latest hydrodynamic (HD) calculations to examine if any SN explosion and environment models are consistent with the X-ray plasma limits. We start with the observations and the data reduction of the SXS in section 2, and present the spectroscopic search results of both the absorption and emission features by the thermal plasma in section 3. In section 4, we derive the upper limits on the physical parameters of the SN and the SNR using both the results presented here and existing results in the literature, and compare with our HD simulations to gain insight into the origin of SN 1054.

2 Observations and data reduction

2.1 Observations

The SXS is a high-resolution X-ray spectrometer based on X-ray micro-calorimetry (Kelley et al. 2016). The HgTe absorbers placed in a 6×6 array absorb individual X-ray photons collected by the X-ray telescope, and the temperature increase of the Si thermometer is read out as a change in its resistance. Because of the very low heat capacity of the sensor controlled at a low temperature of 50 mK, a high spectral resolution is achieved over a wide energy range. The SXS became the first X-ray micro-calorimeter to have made observations of astronomical sources in orbit, and proved its excellent performance despite its short lifetime.

The Crab was observed on 2016 March 25 from 12:35 to 18:01 UT with the SXS. This turned out to be the last data set collected before the tragic loss of the spacecraft the next day. The observation was performed as a part of the calibration program, and we utilize the data to present scientific results in this paper.

Figure 1 shows the $3.'0 \times 3.'0$ field of view on top of a Chandra Advanced CCD Imaging Spectrometer (ACIS) image. The scale corresponds to 1.9 pc at a distance of 2.2 kpc (Manchester et al. 2005). This covers a significant fraction of the observed elliptical nebula with a diameter of 2.9×4.4 pc (Hester 2008). The SXS was still in the commissioning phase (Tsujimoto et al. 2017), and some instrumental setups were non-nominal. Among them, the gate valve status was most relevant for the results presented here. The valve was closed to keep the Dewar in a vacuum on the ground, and was planned to be opened when we
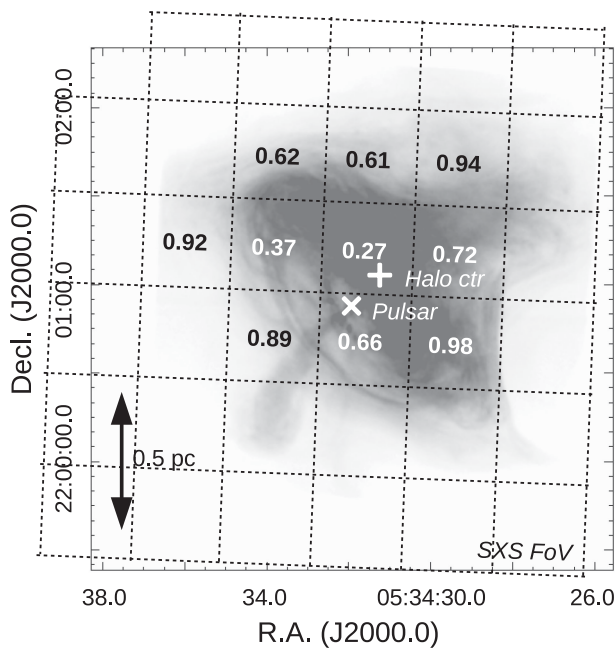
Fig. 1. Field of view of the SXS superimposed on the Chandra ACIS image after correcting for the readout streaks (Mori et al. 2004). The 6 × 6 pixels are shown with the top left corner uncovered for the calibration pixel. The numbers indicate the live time fraction only for pixels less than 0.980. The astrometry of the SXS events can be displaced by 20″6 at 1σ when the star tracker is unavailable. The position of the pulsar (Lobanov et al. 2011) and the halo center (Seward et al. 2006) are respectively shown with the cross and the plus signs.

confirmed the initial outgassing had ceased in the spacecraft. This observation was made before this operation. As a result, the attenuation by a $\sim$260 μm Be window of the gate valve (Eckart et al. 2016) limited the SXS bandpass to above $\sim$2 keV, which would otherwise extend down to $\sim$0.1 keV.

The instrument had reached thermal equilibrium by the time of the observation (Fujimoto et al. 2017; Noda et al. 2017). The detector gain was very stable except for the passage of the South Atlantic anomaly. The previous recycle operation of the adiabatic demagnetization refrigerators was started well before the observation at 10:20 on March 24, and the entire observation was within its 48 hr hold time (Shirron et al. 2016). The energy resolution was 4.9 eV measured with the ^{55}Fe calibration source at 5.9 keV for the full width at half maximum (Porter et al. 2016; Kilbourne et al. 2016; Leutenegger et al. 2016). This superb resolution is not compromised by the extended nature of the Crab nebula for being a non-dispersive spectrometer.

The actual incoming flux measured with the SXS was equivalent to $\sim$0.3 Crab in the 2–12 keV band due to the extra attenuation by the gate valve. The net exposure time was 9.7 ks.

2.2 Data reduction

We started with the cleaned event list produced by the pipeline process version 03.01.005.005 (Angelini et al. 2016). Throughout this paper, we use the HEASoft and CALDB release on 2016 December 22 for the Hitomi collaboration. Further screening against spurious events was applied based on the energy versus pulse rise time. Screening based on the time clustering of multiple events was not applied; it is intended to remove events hitting the out-of-pixel area, but a significant number of false positive detections are expected for high count rate observations like this.

Due to the high count rate, some pixels at the array center suffer dead time (figure 1; Ishisaki et al. 2016). Still, the observing efficiency of $\sim$72% for the entire array is much higher than conventional CCD X-ray spectrometers. For example, Suzaku XIS (Koyama et al. 2007) requires a 1/4 window + 0.1 s burst clocking mode to avoid pile-up for a 0.3 Crab source, and the efficiency is only $\sim$5%. Details of the dead time and pile-up corrections are described in a separate paper. We only mention here that these effects are much less serious for the SXS than CCDs, primarily due to a much faster sampling rate of 12.5 kHz and a continuous readout.

The source spectrum was constructed in the 2–12 keV range at a resolution of 0.5 eV bin^{-1}. Events not contaminated by other events close in time (graded as Hp or Mp; Kelley et al. 2016) were used for better energy resolution. All pixels were combined. The redistribution matrix function was generated by including the energy loss processes from escaping electrons and fluorescent X-rays. The half-power diameter of the telescope is 1″2 (Okajima et al. 2016). The SXS has only a limited imaging capability, and we do not attempt to perform a spatially resolved spectroscopic study in this paper. The SXS does have a timing resolution to resolve the 34 ms pulse phase, but we do not attempt a phase-resolved study either as only a small gain in the contrast of thermal emission against the pulse emission is expected; the unpulsed emission of a $\sim$90% level of averaged count rate can be extracted at a compensation of $\sim$2/3 of the exposure time.

The total number of events in the 2–12 keV range is 7.6 × 10^5. The background spectrum, which is dominated by the non-X-ray background, was accumulated using the data when the telescope was pointed toward the Earth. The non-X-ray background is known to depend on the strength of the geomagnetic field strength at the position of the spacecraft within a factor of a few. The history of the geomagnetic cut-off rigidity during the Crab observation was taken into consideration to derive the background rate

as $8.6 \times 10^{-3}\,\mathrm{s}^{-1}$ in the 2–12 keV band. This is negligible at $\sim 10^{-4}$ of the source rate.

3 Analysis

To search for signatures of thermal plasma, we took two approaches. One is to add a thermal plasma emission model, or to multiply by a thermal plasma absorption model, with the best-fit continuum model with an assumed plasma temperature, which we call plasma search (subsection 3.1). Here, we assume that the feature is dominant either as emission or absorption. The other is a blind search of emission or absorption lines, in which we test the significance of an addition or a subtraction of a line model upon the best-fit continuum model (subsection 3.2). For the spectral fitting, we used the Xspec package version 12.9.0u (Arnaud 1996). The statistical uncertainties are evaluated at 1σ unless otherwise noted.

3.1 Plasma search

3.1.1 Fiducial model

We first constructed the spectral model for the entire energy band. The spectrum was fitted reasonably well with a single power-law model with an interstellar extinction, which we call the fiducial model. Hereafter, all the fitting was performed for unbinned spectra based on the C statistics (Cash 1979). For the extinction model by cold matter, we used the tbabs model version 2.3.2[2] (Wilms et al. 2000). We considered extinction by interstellar gas, molecules, and dust grains, with the parameters fixed at the default values of the model except for the total column density. The SXS is capable of resolving the fine structure of absorption edges, which is not included in the model, except for O K, Ne K, and Fe L edges. This, however, does not affect the global fitting, as the depths of other edges are shallow for the Crab spectrum.

We calculated the effective area assuming a point-like source at the center of the SXS field. The nebula size is no larger than the point spread function. Figure 2 shows the best-fit model, while table 1 summarizes the best-fit parameters for the extinction column by cold matter ($N_{\mathrm{H}}^{(\mathrm{cold})}$), the power-law photon index (Γ), and the X-ray flux (F_{X}). The ratio of the data to the model shows some broad features, which are attributable to the inaccuracies of the calibration including the mirror Au M and L edge features, the gate valve transmission, the line spread function, ray-tracing modeling accuracies, etc. (Tsujimoto et al. 2018). In this paper, therefore, we constrain ourselves to searching for lines that are sufficiently narrow to decouple with these
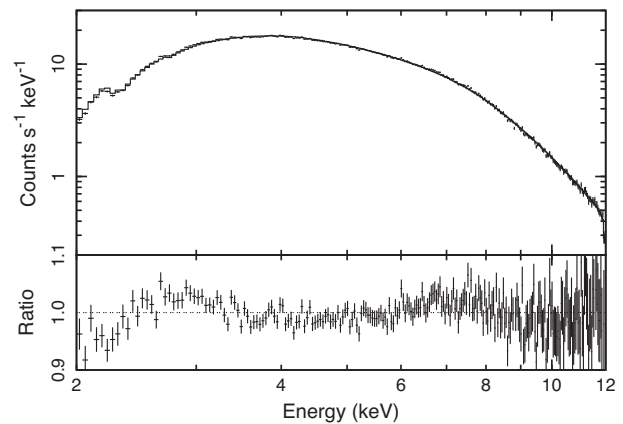
Fig. 2. Best-fit fiducial model to the background-subtracted spectra binned only for display purpose. The top panel shows the data with crosses and the best-fit model with solid lines. The bottom panel shows the ratio to the fit.

Table 1. Best-fit parameters of the global fitting.

Parameter[*]	Best fit
$N_{\mathrm{H}}^{(\mathrm{cold})}$ $10^{21}\,\mathrm{cm}^{-2}$	4.6 (4.1–5.0)
Γ	2.17 (2.16–2.17)
F_{X} erg s^{-1} cm^{-2}[†]	1.722 (1.719–1.728) $\times 10^{-8}$
Red-χ^2/d.o.f.	1.34/19996

[*]The errors indicate a 1σ statistical uncertainty.
[†]The absorption-corrected flux at 2–8 keV.

broad systematic uncertainties. This is possible only with high-resolution spectrometers.

3.1.2 Plasma emission

For the thermal plasma emission, we assumed the optically thin collisional ionization equilibrium (CIE) plasma model and two non-CIE deviations from it. All the calculations were based on the atomic database ATOMDB (Foster et al. 2012) version 3.0.7. We assumed the solar abundance (Wilms et al. 2000). This gives a conservative upper limit for plasma with a super-solar metallicity when they are searched using metallic lines.

First, we used the apec model (Smith et al. 2001) for the CIE plasma, in which the electron, ion, and ionization temperatures are the same. Neither bulk motion nor turbulence broadening was considered, but thermal broadening was taken into account for the lines. For each varying electron temperature (table 2), we selected the strongest emission line in the 10 non-overlapping 1 keV ranges in the 2–12 keV band. For each selected line, we first fitted the ±50 eV range around the line with a power-law model, then added the plasma emission model to set the upper limit of the volume emission measure (Y) of the plasma. Both power-law and plasma emission models were attenuated by an interstellar extinction model of a column density

Table 2. Investigated parameter space.

| Parameter	Unit	Description	Total§	Cases§
T_e	keV	Electron temperature	21	0.1–10 (0.1 dex step)
$\log(n_e t)^*$	s cm^{-3}	Ionization age	8	10.0–13.5 (0.5 step)
$v_i/c^{*\dagger}$		Thermal broadening of lines	5	0.001, 0.002, 0.005, 0.01, 0.02
$\Delta R/R^{\ddagger}$		Shell fraction	6	0.005, 0.01, 0.05, 0.083 (=1/12), 0.10, 0.15

*The parameter is searched only for the plasma emission (sub-subsection 3.1.2).

†The ion type i has a velocity v_i, and thus has a temperature of $T_i = m_i v_i^2/k_B$, in which m_i is the mass of the ion. In the case of Si and Fe, the cases correspond to $T_{Si} < 12$ MeV and $T_{Fe} < 21$ MeV.

‡The value 1/12 is for the self-similar solution (Sedov 1959), and 0.15 follows preceding work (Frail et al. 1995; Seward et al. 2006).

§The adopted parameters (Cases) and the total number of cases (Total) are shown.
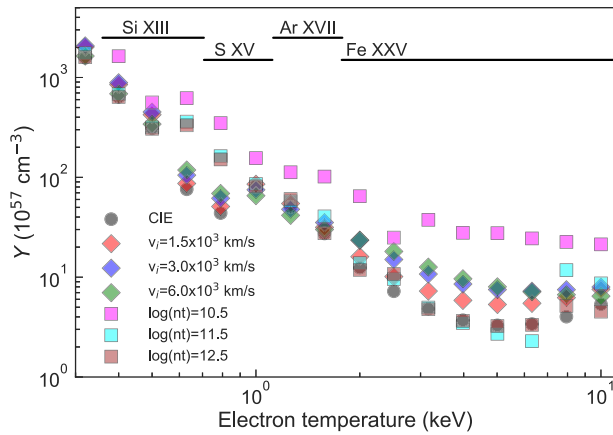
Fig. 3. Three-sigma statistical upper limits of the volume emission measure (Y) for the assumed electron temperature for selected parameters (table 2): (a) CIE, (b) broadened lines by $v_i = (1.5, 3.0, $ and $6.0) \times 10^3$ km s^{-1}, and (c) non-equilibrium cases with $\log(nt$cm^{-3} s$) = 10.5, 11.5,$ and 12.5. The names of the ions giving the strongest emission line for (a) at each temperature are shown at the top. (Color online)

fixed at the fiducial value (table 1). We expect some systematic uncertainty in the $N_H^{(cold)}$ value due to incomplete calibration at low energies. The best-fit value in the fiducial model (table 2) tends to be higher than those in the literature (Kaastra et al. 2009; Weisskopf et al. 2010) by 10%–30%. A 10% decrease in the value leads to <10% decrease of Y for temperatures >1 keV. The normalization of the plasma model was allowed to vary both in the positive and negative directions so as not to distort the significance distribution. The results for selected cases are shown in figure 3.

Deviation from the thermal equilibrium is seen in SNR plasmas (Borkowski et al. 2001; Vink 2012), especially for young SNRs expanding in a low-density environment. We considered two types of deviation. One is non-equilibrium ionization (NEI) using the nei model (Smith & Hughes 2010). This code calculates the collisional ionization as a function of the ionization age ($n_e t$), and accounts for the difference between the ionization and electron temperatures. The electron temperature is assumed constant,

which is reasonable considering that some SNRs show evidence of collision-less instantaneous electron heating at the shock (Yamaguchi et al. 2014b). We took the same procedure with the CIE plasma for the $n_e t$ values listed in table 2, and derived the upper limit of Y.

Another non-CIE deviation is that the electron and ion temperatures are different. More massive ions are expected to have a higher temperature than less massive ions and electrons, and hence are more thermally broadened before reaching equilibrium. We derived the upper limit of Y for several values of the ion's thermal velocity v_i (table 2). In this model, the continuum fit was performed over an energy range of the smaller of the two: $\pm(3 \times Ev_i/c$ or 50) eV centered at the line energy E, so as to decouple the continuum and line fitting when v_i is large.
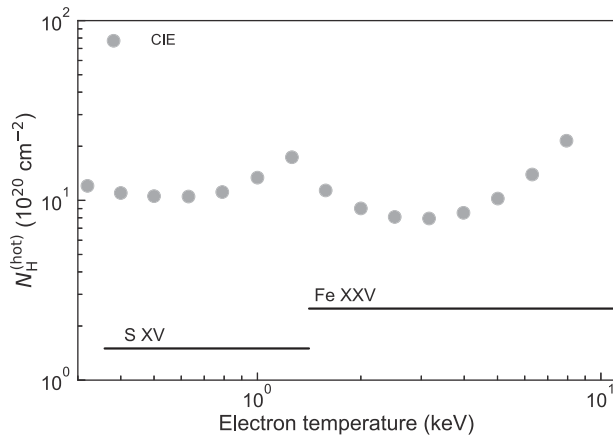
3.1.3 Plasma absorption
A similar approach was taken for deriving the upper limit for the absorption column by a thermal plasma. We used the hotabs model (Kallman & Bautista 2001) and only considered the CIE plasma. At each assumed electron temperature (table 2), we selected the strongest absorption line in the 10 non-overlapping 1 keV ranges in the 2–12 keV band. For each selected line, we first fitted the $\pm$50 eV range around the line with a power-law model, then multiplied the plasma absorption model to set the upper limit of the hydrogen-equivalent absorption column ($N_H^{(hot)}$) by the plasma. The result is shown in figure 4.

3.1.4 Example in the Fe K band
For the emission, the resultant upper limit of Y is less constrained for plasma with lower temperatures. At low temperatures, strong lines are at energies below 2 keV, in which the SXS has no sensitivity as the gate valve was not opened. For increasing temperatures above $\sim$0.5 keV, S-Heα, Ar-Heα, or Fe-Heα are used to set the limit. The most stringent limit is obtained at the maximum formation temperature ($\sim$5 keV) of the Fe-Heα line. For NEI plasma with a low ionization age ($10^{10.5}$ s cm^{-3}), He-like Fe ions have not been

formed yet and thus the limit is not stringent. Conversely, at an intermediate ionization age ($10^{11.5}$ s cm^{-3}), Fe is not fully ionized yet, thus Fe-Heα can give a strong upper limit even for electron temperatures of ~ 10 keV. At $10^{12.5}$ s cm^{-3}, the result is the same with the CIE plasma, as expected.

Figure 5 shows a close-up view of the fitting around the Fe-Heα line for the case of the 3.16 keV electron temperature. Overlaid on the data, models are shown in addition to the best-fit power-law continuum model. Also shown is the expected result by a CCD spectrometer, with which

Fig. 4. Three-sigma statistical upper limits of the hydrogen-equivalent extinction column ($N_{\rm H}^{\rm (hot)}$) by the CIE plasma for the assumed electron temperature. The names of the ions giving the strongest absorption line at each temperature are shown at the bottom.

the levels detectable easily with the SXS would be indistinguishable from the continuum emission. This demonstrates the power of an X-ray micro-calorimeter for weak features from extended sources. The expected energy shifts for a bulk velocity of $\pm 10^3$ km s^{-1}, or ± 22.4 eV, are shown. The data quality is quite similar in this range, thus the result is not significantly affected by a possible gain shift ($\lesssim 1$ eV; Hitomi Collaboration 2016) or a single bulk velocity shift.

3.2 Blind search

We searched for emission or absorption line features at an arbitrary line energy in the 2–12 keV range. We made trials at 20000 energies separated by 0.5 eV. The trials were repeated for a fixed line width corresponding to a velocity of $v = 0, 20, 40, 80, 160, 320, 640$, and 1280 km s^{-1}. For each set of line energy and width, we fitted the spectrum with a power-law model locally in the energy range 3–20 $\sigma_E(E)$ on both sides of the trial energy E. Here, the unit of the fitting range $\sigma_E(E)$ is determined as

$$\sigma_E(E) = \sqrt{[E(v/c)]^2 + [\Delta E_{\rm det}(E)]^2}, \qquad (1)$$

in which $\Delta E_{\rm det}(E)$ is the 1σ width of the Gaussian core of the detector response (Leutenegger et al. 2016). With this variable fitting range, we can test a wide range of line energies and widths. After fixing the best-fit power-law model,
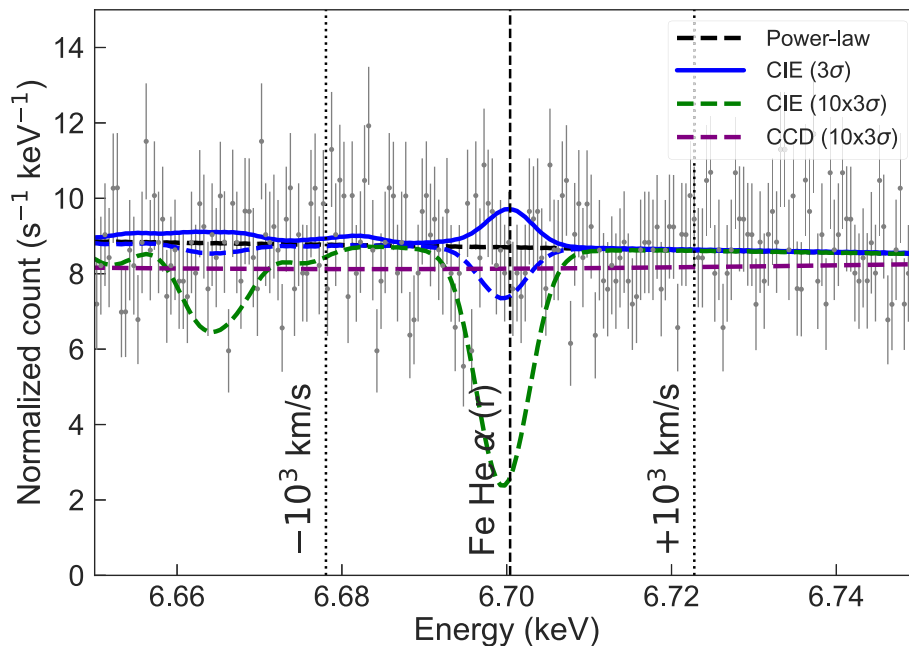
Fig. 5. Close-up view around the Fe-Heα resonance line. Over the unbinned spectrum (gray plus signs), several models are shown: the best-fit continuum model (black dashed), and the emission (solid) and absorption (dashed) by a 3.16 keV CIE plasma with 3σ upper limits (blue) corresponding to $Y = 2.1 \times 10^{57}$ cm^{-3} for emission and $N_{\rm H}^{\rm (hot)} = 7.9 \times 10^{20}$ cm^{-2} for absorption. Ten times the absorption value is also shown in green (SXS) and purple (convolved with a Suzaku XIS response). (Color online)
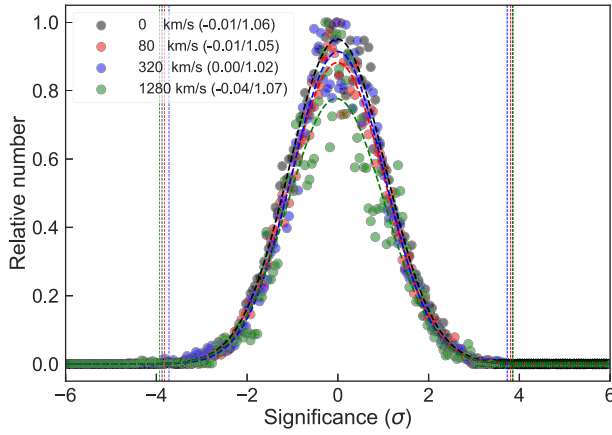
Fig. 6. Distribution of significance [equation (2)] for different assumed velocities in different colors. The distribution is fitted by a single Gaussian model, and its best-fit parameters are shown in the legend as (center/width). The vertical dotted lines indicate the 5σ level of the best-fit Gaussian distribution. (Color online)
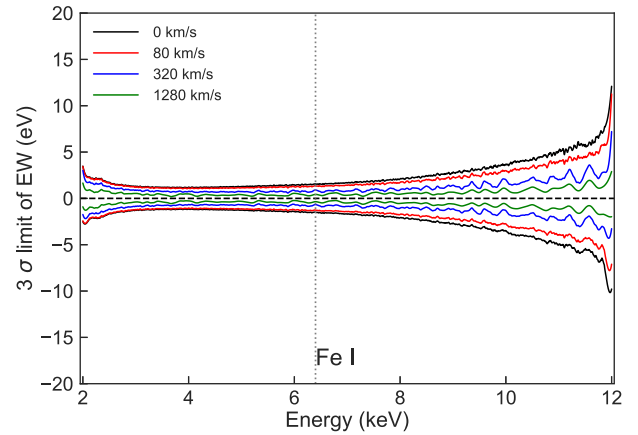

Fig. 7. Three-sigma range of the equivalent width for different assumed velocities. The curves are obtained by convolving the fitting result at each energy bin with a low-pass filter. The structure at 11.9 keV is due to the Au Lα_3 absorption edge by the telescope. (Color online)

we added a Gaussian model allowing both positive and negative amplitudes respectively for emission and absorption lines and refitted in the 0–20 σ_E range on both sides. The detection significance was evaluated as

$$\sigma = \frac{N_{\mathrm{line}}}{\sqrt{\Delta N_{\mathrm{line}}^2 + (N_{\mathrm{line}} \Delta I_{\mathrm{cont}}/I_{\mathrm{cont}})^2}}, \tag{2}$$

in which N_{line} and ΔN_{line} are the best-fit and 1σ statistical uncertainty of the line normalization in units of s^{-1} cm^{-2}, whereas I_{line} and ΔI_{line} are those of the continuum intensity in units of s^{-1} cm^{-2} keV^{-1} at the line energy.

Figure 6 shows the distribution of the significance. All are reasonably well fitted by a single Gaussian distribution. We tested several different choices of fitting ranges and confirmed that the overall result does not change. Above a 5σ level (0.01 false positives expected for 20000 trials) of the best-fit Gaussian distribution, no significant detection was found except for (1) several detections of absorption in the 2.0–2.2 keV energy range for a wide velocity range, and (2) a detection of absorption at $\sim$9.48 keV for 160 and 320 km s^{-1}. The former is likely due to the inaccurate calibration of the Au M edges of the telescope. For the latter, no instrumental features or strong atomic transitions are known around this energy. However, we do not consider this to be robust as it escapes detection only by changing the fitting ranges.

The equivalent width, EW $= N_{\mathrm{line}}/I_{\mathrm{cont}}$, was derived for every set of the line energy and width along with their 3σ statistical uncertainty (figure 7). The 3σ limit of EW at 6.4 keV is $\lesssim 2$ eV. We would expect the Fe fluorescence line with EW $= \alpha(\Delta\Omega/4\pi)(N_{\mathrm{H}}^\gamma/10^{22}\,\mathrm{cm}^{-2})$ eV, in which $\alpha \sim 2.8$ for the Crab's power-law spectrum (Krolik & Kallman 1987). $\Delta\Omega$ and N_{H}^γ are, respectively, the subtended

angle and the H-equivalent column of the fluorescing matter around the incident emission. Assuming $\Delta\Omega = 4\pi$ and $N_{\mathrm{H}}^\gamma < 0.32 \times 10^{22}$ cm^{-2}, which is the measured value in the line of sight inclusive of the ISM (Mori et al. 2004), the expected EW is consistent with the upper limit by the SXS.

4 Discussion

In subsection 4.1, we convert the upper limit of Y or $N_{\mathrm{H}}^{(\mathrm{hot})}$ with the SXS into that of the plasma density (n_{X}) by making several assumptions. In subsection 4.2, we re-evaluate the data by other methods in the literature under the same assumptions to assemble the most stringent upper limit of n_{X} for various ranges of the parameters. In subsection 4.3, we perform an HD calculation for some SN models and verify that the searched parameter ranges are reasonable. In subsection 4.4, we compare the HD result with observed limits.

4.1 Constraints on the plasma density with SXS

To convert the upper limits of Y and $N_{\mathrm{H}}^{(\mathrm{hot})}$ of the thermal plasma into those of the X-ray emitting plasma density (n_{X}), we assume the plasma is uniform in a spherically symmetric shell in a range of R to $R + \Delta R$ from the center. We assumed several shell fraction ($\Delta R/R$) values (table 2). For simplicity, the electron and ion densities are the same, and all ions are hydrogen. This gives a conservative upper limit for the plasma mass.

We first use the upper limit of the plasma emission. The density is $n_{\mathrm{X}} = \sqrt{Y/V_{\mathrm{obs}}}$, in which V_{obs} is the observed emitting volume. Some selected cases are shown in figure 8 (thick solid and dashed curves). If the SXS square field of view with $\theta_{\mathrm{SXS}} = 3'.0$ covers the entire shell at $R < 3'.0$,
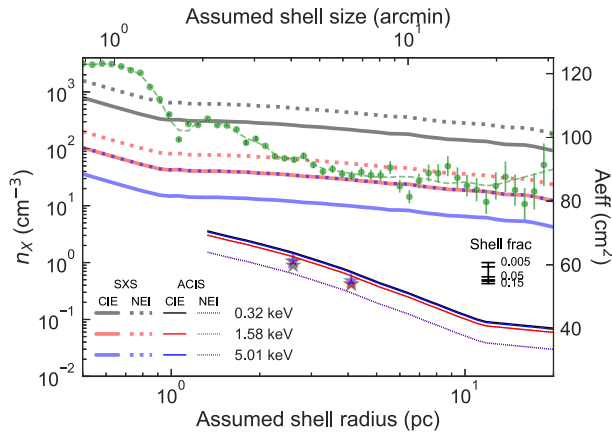
Fig. 8. Upper limits to the plasma density for several selected electron temperatures of CIE (solid) and NEI with $n_e t = 10^{10.5}$ s cm^{-3} (dotted) plasmas as a function of the assumed shell radius for the SXS (thick) and ACIS (thin; Seward et al. 2006) when the shell fraction is $\Delta R/R = 0.05$. The observed limits move vertically when the shell fraction is changed by the scaling shown in the figure. The effective area for the projected shell distribution is shown with green points with statistical uncertainties by the ray-tracing simulations, which is smoothed (green dashes) by the Savitzky and Golay (1964) method to use for the correction. The star marks are the expected limits with off-source pointing with the SXS at 2.6 and 4.1 pc for CIE of different temperatures. (Color online)

Fig. 9. Upper limits to the plasma density for several selected electron temperatures of a CIE plasma as a function of the assumed shell radius for the SXS (thick) and RGS (thin; Kaastra et al. 2009) when the shell fraction is $\Delta R/R = 0.05$. The observed limits move vertically when the shell fraction is changed by the scaling shown in the figure. Also shown is the upper limit by a radio dispersion measure (DM) of the Crab pulsar (Lundgren et al. 1995). (Color online)

$V_{\rm obs} \sim 4\pi R^2 \Delta R$. If the field is entirely contained in the shell at $R > 2.'1$, $V_{\rm obs}$ should be replaced with $\sim (D\theta_{\rm SXS})^2 \Delta R$, in which D is the distance to the source. These approximations at the two ends make a smooth transition.

Here, we made a correction for the reduced effective area for the extended structure of the shell. As R increases within the SXS field of view, the effective area averaged over the view decreases as more photons are close to the field edges. This effect is small in the case of the Crab because the central pixels suffer dead time due to the high count rate (figure 1). In fact, a slightly extended structure up to $R \sim 1.'2$ has a larger effective area than a point-like distribution. As R increases beyond the field, the emission within the field becomes closer to a flat distribution, and the reduction of the effective area levels off (figure 8; green data and dashed curve).

Next, we convert the upper limits by the extinction column to the density with $n_{\rm X} = N_{\rm H}^{\rm (hot)} / \Delta R$, which is shown in figure 9 (thick lines). We assume that the absorption feature is superimposed on a point-like continuum source, and thus no correction was made for the extended structure.

4.2 Results with other techniques

We compare the results with previous work using three different techniques. First, Seward, Tucker, and Fesen (2006) used the Advanced CCD Imaging Spectrometer (ACIS: Garmire et al. 2003) on board the Chandra X-ray Observatory (Weisskopf et al. 2002) with an unprecedented imaging

resolution, and derived an upper limit for the thermal emission assuming that it would be detectable if it has a 0.1 times surface brightness of the observed halo emission attributable to the dust scattering. We re-evaluated their raw data (their figure 5) under the same assumptions as SXS (figure 8; thin solid and dashed curves). No ACIS limit was obtained below $R \sim 2'$ due to the extreme brightness of the PWN. Beyond $R \sim 18'$, at which there is no ACIS measurement, we used the upper limit at $18'$. For the ACIS limits, a more stringent limit is obtained for the NEI case with a low ionization age ($10^{10.5}$ s cm^{-3}) than the CIE case with the same temperature. This is because the Fe L series lines are enhanced for such NEI plasmas and the ACIS is sensitive also at <2 keV, unlike the SXS with the gate valve closed.

Second, Kaastra et al. (2009) presented the Crab spectrum using the Reflecting Grating Spectrometer (RGS: den Herder et al. 2001) on board the XMM-Newton Observatory (Jansen et al. 2001). For the non-thermal emission of the PWN, they reported a detection of the absorption feature by the O-Heα and O-Lyα lines respectively at 0.58 and 0.65 keV with a similar equivalent width of ~ 0.2 eV, assuming that the lines are narrow. The former was also confirmed in the Chandra Low Energy Transmission Grating data. However, these absorption lines are often seen in the spectra of Galactic X-ray binaries (e.g., Yao & Wang 2006), which is attributed to the hot gas in the interstellar medium with a temperature of a few MK. Adopting the value of Sakai et al. (2014), the expected column density by such a gas for the Crab is $\sim 8 \times 10^{18}$ cm^{-2}, which is non-negligible. We therefore consider that the values measured with RGS are an upper limit for the plasma around
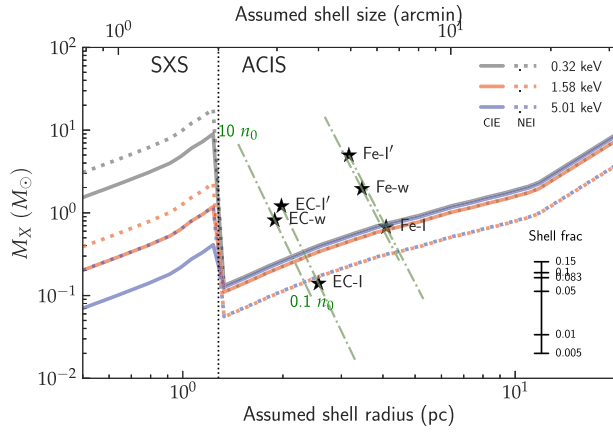
Fig. 10. Upper limit of the total plasma mass when the shell has a size R for several electron temperatures of CIE (solid) and NEI with $n_e t = 10^{10.5}\,\mathrm{s\,cm^{-3}}$ (dotted) plasmas. $\Delta R/R = 0.05$ is assumed. The observed limits move vertically when the shell fraction is changed by the scaling shown in the figure. The position of $(R_{\mathrm{CD}}, \overline{M_X})$ is shown for the models in table 3 with the stars, and their direction of change when n_0 is changed by a factor of 10 or 0.1 (dotted-and-dashed green lines from the stars). (Color online)

the Crab. Using the same assumptions with SXS, we re-evaluated the RGS limit (thin lines in figure 9).

Third, the dispersion measure from the Crab pulsar reflects the column density of ionized gas along the line of sight. This includes not only the undetected thermal plasma around the Crab but also the hot and warm interstellar gas. Lundgren et al. (1995) derived a measure of $1.8 \times 10^{20}\,\mathrm{cm^{-2}}$, which converts to another density limit (dashed line in figure 9).

We now have the upper limit for n_X for several sets of R, ΔR, and T by assembling the lowest values among various methods (re-)evaluated under the same assumptions. We convert the limit to that of the total X-ray emitting mass $M_X = n_X m_p V_{\mathrm{tot}}$, where m_p is the proton mass and V_{tot} is the total emitting volume for an assumed shell size and fraction. The resultant limit is shown in Figure 10. The most stringent limit is given by the emission search either by ACIS or SXS. The SXS result complements the ACIS result at $R < 1.3\,\mathrm{pc}$, and the two give an upper limit of $\sim 1\,M_\odot$ for the X-ray-emitting plasma at any shell radius. The exception is for low plasma temperatures below $\sim 1\,\mathrm{keV}$, for which the SXS with the closed gate valve yields a less constraining limit.

4.3 Hydrodynamic calculation

We performed HD calculations to verify that the searched parameter ranges (table 2) are reasonable and to confirm if there are any SN models consistent with the observed limit. We used the *CR-hydro-NEI* code (Lee et al. 2014 and references therein), which calculates time-dependent, non-equilibrium plasma in one dimension. At the forward

shock, the kinetic energy is thermalized independently for each species, thus the temperature is proportional to the mass of the species. The plasma is then thermally relaxed by the Coulomb interaction. No collisionless shocks are included. Energy loss by radiation is included, while that by cosmic rays is omitted.

We considered two SN explosion models under two circumstellar environments (table 3) as representatives. The former two are (a) an Fe-core-collapse SN with a red super-giant progenitor with the initial explosion energy $E_0 = 1.21 \times 10^{51}\,\mathrm{erg}$ and ejecta mass $M_{\mathrm{ej}} = 12.1\,M_\odot$ (Patnaude et al. 2015), and (b) an EC SN with a super AGB progenitor with $E_0 = 0.15 \times 10^{51}\,\mathrm{erg}$ and $M_{\mathrm{ej}} = 4.36\,M_\odot$ (Moriya et al. 2014). The latter two are (1) uniform density of $n_0 = 0.1\,\mathrm{cm^{-3}}$, and (2) the density profile of the progenitor wind: $n_0(r) = \dot{M}_{\mathrm{wind}}/(4\pi v_{\mathrm{wind}} m_p r^2)$, with mass loss rate $\dot{M}_{\mathrm{wind}} = 1 \times 10^{-5}\,M_\odot\,\mathrm{yr^{-1}}$ and wind velocity $v_{\mathrm{wind}} = 20\,\mathrm{km\,s^{-1}}$ (Moriya et al. 2014). For the wind density parameter (Chugai & Danziger 1994), $w = \dot{M}_{\mathrm{wind}}/v_{\mathrm{wind}} = 3.2 \times 10^{14}\,\mathrm{g\,cm^{-1}}$.

The 2×2 models are labeled as (a-1) Fe-I, (a-2) Fe-w, (b-1) EC-I, and (b-2) EC-w. For the Fe-I and EC-I models, we also calculated an elevated ISM density of $n_0 = 1.0\,\mathrm{cm^{-3}}$ (respectively labeled as Fe-I′ and EC-I′). For all these models, we assumed the power (n_{ej}) of the unshocked ejecta density as a function of velocity to be 9 (Fransson et al. 1996). Only for the model EC-w, we calculated with $n_{\mathrm{ej}} = 7$ to see the effect of this parameter (labeled as EC-w″).

Table 3 summarizes the SN setup stated above and the SNR outcome at an age of 962 yr, which includes the radius of the forward shock (FS), contact discontinuity (CD), and reverse shock (RS) (R_{FS}, R_{CD}, and R_{RS}), the velocity of the forward and reverse shocks (v_{FS} and v_{RS}), the mass between CD and FS ($M_{\mathrm{CD\text{-}FS}}$) and that between RS and CD ($M_{\mathrm{RS\text{-}CD}}$). The two masses represent the shocked ISM and ejecta, respectively. The radius is close to the observed size of the optical photo-ionized nebula, and the radii and velocities match reasonably well with analytical approaches (Chevalier 1982; Truelove & McKee 1999) within 10%, which validates our calculation. The RS radius is larger than the X-ray emitting synchrotron nebula, which justifies that our calculation does not include the interaction with it.

From these, we calculated $(R_{\mathrm{RS}} - R_{\mathrm{CD}})/R_{\mathrm{CD}}$ as a proxy for the shell fraction, $3\mu m_p v_{\mathrm{FS}}^2/16$ as a proxy for the electron temperature after Coulomb relaxation, in which $\mu = 0.5$ is the mean molecular weight, and the unshocked ejecta mass $M_{\mathrm{unshocked}} = M_{\mathrm{ej}} - M_{\mathrm{RS\text{-}CD}}$. We also derived the average of the electron and Fe temperatures ($\overline{T_e}$ and $\overline{T_{\mathrm{Fe}}}$) and the ionization age ($\overline{n_e t}$) weighted over the absorbed X-ray flux. The X-ray emitting mass ($\overline{M_X}$) was estimated by integrating the mass with a temperature in excess of $\overline{T_e}$.

Table 3. Results of HD calculation.

Label	Fe-I	Fe-I′	Fe-w	EC-I	EC-I′	EC-w	EC-w″
SN setup:							
SN explosion	Fe	Fe	Fe	EC	EC	EC	EC
E_0 (10^{51} erg)	1.21	1.21	1.21	0.15	0.15	0.15	0.15
M_{ej} ($M_\odot$)	12.1	12.1	12.1	4.36	4.36	4.36	4.36
n_{ej}	9	9	9	9	9	9	7
Environment	ISM	ISM	wind	ISM	ISM	wind	wind
n_0 (cm^{-3})	0.1	1.0	–	0.1	1.0	–	–
$w = \dot{M}_{wind}/v_{wind}$ (10^{14} g cm^{-1})	–	–	3.2	–	–	3.2	3.2
SNR outcome:							
R_{FS} (pc)	4.6	3.6	4.3	2.9	2.2	2.3	2.6
R_{CD} (pc)	4.1	3.2	3.5	2.6	2.0	1.9	2.0
R_{RS} (pc)	3.8	2.9	3.3	2.4	1.8	1.8	1.9
v_{FS} (10^3 km s^{-1})	3.1	2.4	3.7	2.0	1.5	2.0	2.1
v_{RS}* (10^3 km s^{-1})	1.4	1.2	0.51	0.88	0.68	0.29	0.39
$M_{CD\text{-}FS}$ ($M_\odot$)	1.4	6.6	2.0	0.35	1.6	1.1	1.2
$M_{RS\text{-}CD}$ ($M_\odot$)	1.8	7.0	4.1	0.42	2.2	2.2	1.3
				— Derived values —			
$\frac{R_{CS}-R_{RS}}{R_{CD}}$	0.07	0.07	0.04	0.06	0.09	0.04	0.07
$\frac{3}{16}\mu m_p v_{FS}^2$ (keV)	9.4	5.7	13	3.8	2.2	4.0	4.1
$M_{unshocked}$ ($M_\odot$)	10	5.1	8.0	3.9	2.2	2.2	3.0
			— Absorbed X-ray flux weighted average —				
$\overline{T_e}$ (keV)	1.0	1.6	0.51	0.71	0.95	0.74	0.51
$\overline{T_{Fe}}$ (keV)	130	26	50	57	4.0	62	90
$\overline{n_e t}$ (10^{11} cm s^{-1})	0.21	1.5	9.9	0.22	1.59	11.8	10.2
$\overline{M_X}$ ($M_\odot$)	0.67	5.0	2.0	0.14	1.2	0.81	1.1

*Velocity with respect to the ejecta.

The ranges searched for all parameters (table 2) encompass the HD result for all models. The electron temperature is expected between $3\mu m_p v_{FS}^2/16$ and $\overline{T_e}$; the former is the highest for thermalizing all the kinetic energy instantaneously, while the latter is the lowest for starting the Coulomb relaxation without collisionless heating. The averaged Fe temperature $\overline{T_{Fe}}$ is sufficiently low to consider that the line is relatively narrow; the thermal broadening by this is 32 eV at 6.7 keV for $\overline{T_{Fe}} = 130$ keV. The ionization age ($n_e t$) ranges over two orders from 10^{10} to 10^{12} cm^{-3} s^{-1}, depending on the pre-explosion environment, where the wind density cases result in higher values than the ISM density cases.

4.4 Comparison with observed limits

Finally, we compare the HD results with observation in figure 10. For the radius and the X-ray plasma mass, we plotted (R_{CD}, $\overline{M_X}$) in table 3. The shell size by the models (R_{CD}) is larger than 1.3 pc, where we have a stringent limit on M_X with the observations. The HD results depend on the choice of the parameters in the SN setup (E_0, M_{ej}, n_0 or w, and n_{ej}; table 3). We can estimate in which direction the

model points move in the plot when these parameters are changed.

First, the two parameters E_0 and M_{ej} are known to be correlated in type II SNe. Our two SN models are in line with the relation by Pejcha and Prieto (2015). Therefore, the model points move roughly in the direction of the lines connecting the EC-I and Fe-I models, or the EC-w and Fe-w models. For a fixed explosion energy of 1.21×10^{51} erg for our Fe model, a plausible range of M_{ej} is 12–32 $M_\odot$ (Pejcha & Prieto 2015), and thus our model is close to the lower bound. Second, for n_0, the points move in parallel with the lines connecting Fe-I and Fe-I′ or EC-I and EC-I′. This should be the same for w in the wind environment case. Third, for n_{ej}, there is little difference between the results of the Fe-w and Fe-w″ models, so we consider that this parameter does not affect the result very much. In terms of the comparison with the observation limit, n_0 or w is the most important factor.

Although the small observed mass of the Crab is argued to rule out an Fe-core-collapse SN as its origin (Seward et al. 2006), we consider that this does not simply hold. Our models illustrate that such a small mass can be reproduced if an Fe-core-collapse SN explosion takes place in a

sufficiently low-density environment with ISM density $n_0 \lesssim$ 0.03 cm^{-3} (Fe-I) or wind density parameter $w \lesssim 10^{14}$ g cm^{-1} (Fe-w). In such a case, a large fraction of the ejecta mass is unshocked (table 3) and escapes from detection. Some of the unshocked ejecta may be visible when they are photo-ionized by the emission from the PWN to a $\approx 10^3$ K gas (Fesen et al. 1997) or a $\approx 10^4$ K gas (Sollerman et al. 2000).

We argue that both the Fe and EC models still hold as compatible with the observed mass limits. In either case, it is strongly preferred that the pre-explosion environment is low in density; i.e., $n_0 \lesssim 0.1$ cm^{-3} (EC-I) or $\lesssim 0.03$ cm^{-3} (Fe-I) for the ISM environment or $w \lesssim 10^{14}$ g cm^{-1} for the wind environment (both Fe-w and EC-w). For the latter, a large w value (e.g., 6×10^{18} g cm^{-1}; Smith 2013), which is an idea to explain the initial brightness of SN 1054, is not favored. In fact, such a low-density environment is suggested by observations. At the position of the Crab, which is off-plane in the anti-Galactic center direction, the ISM density is ~ 0.3 cm^{-3} by a Galactic model (Ferrière 1998). Wallace et al. (1999) further claimed the presence of a bubble around the Crab based on an HI mapping with a density lower than the surroundings. Our result suggests that SN 1054 took place in such a low-n_0 environment and a wind environment from its progenitor of a low wind density value.

5 Conclusion

We utilized the SXS calibration data of the Crab nebula in 2–12 keV to set an upper limit on the thermal plasma density by spectroscopically searching for emission or absorption features in the Crab spectrum. No significant emission or absorption features were found in either the plasma or the blind searches.

Along with the data in the literature, we evaluated the result under the same assumptions to derive the X-ray plasma mass limit to be $\lesssim 1 M_\odot$ for a wide range of assumed shell radii (R) and plasma temperatures (T). The SXS sets a new limit in $R < 1.3$ pc for $T > 1$ keV. We also performed HD simulations of the Crab SNR for two SN explosion models under two pre-explosion environments. Both SN models are compatible with the observed limits when the pre-explosion environment has a low density of $\lesssim$ 0.03 cm^{-3} (Fe model) or $\lesssim 0.1$ cm^{-3} (EC model) for the uniform density, or $\lesssim 10^{14}$ g cm^{-1} ($\dot{M}_{wind} \lesssim 3 \times 10^{-6}$ $M_\odot$ yr^{-1} for $v_{wind} = 20$ km s^{-1}) for the wind density parameter in the wind environment.

A low-energy explosion is favored based on the abundance, initial light curve, and nebular size studies (MacAlpine & Satterfield 2008; Moriya et al. 2014; Yang & Chevalier 2015). We believe that a positive detection of

thermal plasma, in particular with lines, is key to distinguishing the Fe and EC models. It is worth noting that the observed limit is close to the model predictions. We now know the high potential of a spectroscopic search with the SXS, and may expect a detection of the thermal feature by placing the SXS field center at several offset positions. With a 10 ks snapshot at four different positions at the radius of the EC-I and Fe-I models (respectively 2.6 and 4.1 pc), an upper limit lower than that with ACIS by a factor of a few is expected (figure 8).

This was exactly what was planned next. If it were not for the loss of the spacecraft, estimated to have happened at 1:42 UT on 2016 March 26, a series of offset Crab observations should have started 8 hr later for calibration purposes, which should have been followed by the gate valve opening to allow access down to 0.1 keV. The eight hours has now turned into many years, but we should be back as early as possible.

Author contributions

M. Tsujimoto led this study in data analysis and writing drafts. He also contributed to the SXS hardware design, fabrication, integration and tests, launch campaign, in-orbit operation, and calibration. S.-H. Lee performed the hydro-dynamic calculations and their interpretation for this paper. K. Mori and H. Yamaguchi contributed to discussions on SNRs. They also made hardware and software contributions to the Hitomi satellite. N. Tominaga and T. J. Moriya gave critical comments on SNe. T. Sato worked for the tele-scope response on data analysis and calibration. C. de Vries led the filter wheel of the SXS, which gave the only pixel-to-pixel gain reference of this spectrometer in orbit. R. Iizuka contributed to the testing and calibration of the telescope, and the operation of the SXS. A. R. Foster and T. Kallman helped with the plasma models. M. Ishida, R. F. Mushotzky, A. Bamba, R. Petre, B. J. Williams, S. Safi-Harb, A. C. Fabian, C. Pinto, L. C. Gallo, E. M. Cackett, J. Kaastra, M. Ozaki, J. P. Hughes, and D. McCammon improved the draft.

References

Angelini, L., et al. 2016, Proc. SPIE, 9905, 990514

Arnaud, K. A. 1996, in ASP Conf. Ser., 101, Astronomical Data Analysis Software and Systems V, ed. G. H. Jacoby & J. Barnes (San Francisco: ASP), 17

Baade, W., & Zwicky, F. 1934, Proc. Natl. Acad. Sci. USA, 20, 254

Bamba, A., Mori, K., & Shibata, S. 2010, ApJ, 709, 507

Borkowski, K. J., Lyerly, W. J., & Reynolds, S. P. 2001, ApJ, 548, 820

Cash, W. 1979, ApJ, 228, 939

Chevalier, R. A. 1977, in Supernovae, ed. D. N. Schramm (Dordrecht: D. Reidel Publishing Co.), 53

Chevalier, R. A. 1982, ApJ, 258, 790

Chugai, N. N., & Danziger, I. J. 1994, MNRAS, 268, 173

Davidson, K., & Fesen, R. A. 1985, ARA&A, 23, 119

den Herder, J. W., et al. 2001, A&A, 365, L7

Eckart, M. E., et al. 2016, Proc. SPIE, 9905, 99053W

Ferrand, G., & Safi-Harb, S. 2012, Adv. Space Res., 49, 1313

Ferrière, K. 1998, ApJ, 497, 759

Fesen, R. A., Shull, J. M., & Hurford, A. P. 1997, AJ, 113, 354

Foster, A. R., Ji, L., Smith, R. K., & Brickhouse, N. S. 2012, ApJ, 756, 128

Frail, D. A., Kassim, N. E., Cornwell, T. J., & Goss, W. M. 1995, ApJ, 454, L129

Fransson, C., Lundqvist, P., & Chevalier, R. A. 1996, ApJ, 461, 993

Fujimoto, R., et al. 2017, J. Astron. Telesc. Inst. Syst., 4, 011208

Garmire, G. P., Bautz, M. W., Ford, P. G., Nousek, J. A., & Ricker, G. R., Jr. 2003, Proc. SPIE, 4851, 28

Hester, J. J. 2008, ARA&A, 46, 127

Hitomi Collaboration 2016, Nature, 535, 117

Hughes, J. P., et al. 1995, ApJ, 444, L81

Ishisaki, Y., et al. 2016, Proc. SPIE, 9905, 99053T

Jahoda, K., Markwardt, C. B., Radeva, Y., Rots, A. H., Stark, M. J., Swank, J. H., Strohmayer, T. E., & Zhang, W. 2006, ApJS, 163, 401

Janka, H.-T., Müller, B., Kitaura, F. S., & Buras, R. 2008, A&A, 485, 199

Jansen, F., et al. 2001, A&A, 365, L1

Kaastra, J. S., de Vries, C. P., Costantini, E., & den Herder, J. W. A. 2009, A&A, 497, 291

Kallman, T., & Bautista, M. 2001, ApJS, 133, 221

Kargaltsev, O., Durant, M., Pavlov, G. G., & Garmire, G. 2012, ApJS, 201, 37

Kelley, R. L., et al. 2016, Proc. SPIE, 9905, 99050V

Kilbourne, C. A., et al. 2016, Proc. SPIE, 9905, 99053L

Kirsch, M. G., et al. 2005, Proc. SPIE, 5898, 22

Kitaura, F. S., Janka, H.-T., & Hillebrandt, W. 2006, A&A, 450, 345

Koyama, K., et al. 2007, PASJ, 59, S23

Krolik, J. H., & Kallman, T. R. 1987, ApJ, 320, L5

Lee, S.-H., Patnaude, D. J., Ellison, D. C., Nagataki, S., & Slane, P. O. 2014, ApJ, 791, 97

Leutenegger, M. A., et al. 2016, Proc. SPIE, 9905, 99053U

Lobanov, A. P., Horns, D., & Muxlow, T. W. B. 2011, A&A, 533, A10

Lovelace, R. B. E., Sutton, J. M., & Craft, H. D. 1968, IAU Circ., 2113

Lundgren, S. C., Cordes, J. M., Ulmer, M., Matz, S. M., Lomatch, S., Foster, R. S., & Hankins, T. 1995, ApJ, 453, 433

Lundmark, K. 1921, PASP, 33, 225

MacAlpine, G. M., & Satterfield, T. J. 2008, AJ, 136, 2152

Madsen, K. K., et al. 2015, ApJ, 801, 66

Manchester, R. N., Hobbs, G. B., Teoh, A., & Hobbs, M. 2005, AJ, 129, 1993

Mattana, F., et al. 2009, ApJ, 694, 12

Mauche, C. W., & Gorenstein, P. 1985, in The Crab Nebula and Related Supernova Remnants, ed. M. C. Kafatos & R. B. C. Henry (Cambridge: Cambridge University Press), 81

Mori, K., Burrows, D. N., Hester, J. J., Pavlov, G. G., Shibata, S., & Tsunemi, H. 2004, ApJ, 609, 186

Moriya, T. J., Tominaga, N., Langer, N., Nomoto, K., Blinnikov, S. I., & Sorokina, E. I. 2014, A&A, 569, A57

Ng, C.-Y., & Romani, R. W. 2008, ApJ, 673, 411

Noda, H., et al. 2017, J. Astron. Telesc. Inst. Syst., 4, 011202

Nomoto, K., Sugimoto, D., Sparks, W. M., Fesen, R. A., Gull, T. R., & Miyaji, S. 1982, Nature, 299, 803

Okajima, T., et al. 2016, Proc. SPIE, 9905, 99050Z

Patnaude, D. J., Lee, S.-H., Slane, P. O., Badenes, C., Heger, A., Ellison, D. C., & Nagataki, S. 2015, ApJ, 803, 101

Pejcha, O., & Prieto, J. L. 2015, ApJ, 806, 225

Porter, F. S., et al. 2016, Proc. SPIE, 9905, 99050W

Possenti, A., Cerutti, R., Colpi, M., & Mereghetti, S. 2002, A&A, 387, 993

Predehl, P., & Schmitt, J. H. M. M. 1995, A&A, 293, 889

Rudie, G. C., Fesen, R. A., & Yamada, T. 2008, MNRAS, 384, 1200

Sakai, K., Yao, Y., Mitsuda, K., Yamasaki, N. Y., Wang, Q. D., Takei, Y., & McCammon, D. 2014, PASJ, 66, 83

Savitzky, A., & Golay, M. J. E. 1964, Anal. Chem., 36, 1627

Sedov, L. I. 1959, Similarity and Dimensional Methods in Mechanics (New York: Academic Press)

Seward, F. D., Gorenstein, P., & Smith, R. K. 2006, ApJ, 636, 873

Shirron, P. J., et al. 2016, Proc. SPIE, 9905, 99053O

Smith, N. 2013, MNRAS, 434, 102

Smith, R. K., Brickhouse, N. S., Liedahl, D. A., & Raymond, J. C. 2001, ApJ, 556, L91

Smith, R. K., & Hughes, J. P. 2010, ApJ, 718, 583

Sollerman, J., Kozma, C., & Lundqvist, P. 2001, A&A, 366, 197

Sollerman, J., Lundqvist, P., Lindler, D., Chevalier, R. A., Fransson, C., Gull, T. R., Pun, C. S. J., & Sonneborn, G. 2000, ApJ, 537, 861

Staelin, D. H., & Reifenstein, E. C., III 1968, Science, 162, 1481

Stephenson, F. R., & Green, D. A. 2002, Historical Supernovae and their Remnants (Oxford: Clarendon Press)

Takahashi, T., et al. 2016, Proc. SPIE, 9905, 99050U

Terada, Y., et al. 2008, PASJ, 60, S25

Tominaga, N., Blinnikov, S. I., & Nomoto, K. 2013, ApJ, 771, L12

Truelove, J. K., & McKee, C. F. 1999, ApJS, 120, 299

Tsujimoto, M., et al. 2017, J. Astron. Telesc. Inst. Syst., 4, 011205

Tsujimoto, M., et al. 2018, PASJ, 70, 20

Tziamtzis, A., Schirmer, M., Lundqvist, P., & Sollerman, J. 2009, A&A, 497, 167

Vink, J. 2012, A&AR, 20, 49

Wallace, B. J., Landecker, T. L., Kalberla, P. M. W., & Taylor, A. R. 1999, ApJS, 124, 181

Weisskopf, M. C., Brinkman, B., Canizares, C., Garmire, G., Murray, S., & Van Speybroeck, L. P. 2002, PASP, 114, 1

Weisskopf, M. C., Guainazzi, M., Jahoda, K., Shaposhnikov, N., O'Dell, S. L., Zavlin, V. E., Wilson-Hodge, C., & Elsner, R. F. 2010, ApJ, 713, 912

Wilms, J., Allen, A., & McCray, R. 2000, ApJ, 542, 914

Yamaguchi, H., et al. 2014a, ApJ, 785, L27

Yamaguchi, H., et al. 2014b, ApJ, 780, 136

Yang, H., & Chevalier, R. A. 2015, ApJ, 806, 153

Yao, Y., & Wang, Q. D. 2006, ApJ, 641, 930